

Simulations of Horizontal Roll Vortex Development Above Lines of Extreme Surface Heating

W. E. Heilman¹ and J. D. Fast²

¹USDA Forest Service, 1407 South Harrison Road, East Lansing, MI 48823 USA

²Westinghouse Savannah River Company, Savannah River Laboratory, Aiken, SC 29808 USA

¹Tel. 517 355-7740; Fax 517 355-5121

²Tel. 803 725-3256; Fax 803 725-4233

Abstract. A two-dimensional, nonhydrostatic, coupled, earth/atmospheric model has been used to simulate mean and turbulent atmospheric characteristics near lines of extreme surface heating. Prognostic equations are used to solve for the horizontal and vertical wind components, potential temperature, and turbulent kinetic energy (TKE). The model computes nonhydrostatic pressure deviations from a derived atmospheric continuity equation. Horizontal pressure gradients generated from surface heating are calculated from thermal wind principles.

Model simulations indicate the development of buoyancy-induced horizontal roll vortices near regions with surface temperatures typical of wildland fires. Model results are qualitatively similar to previous wind-tunnel experiments. When surface temperatures are increased, the circulations associated with the roll vortices become more vigorous. The introduction of a weak ambient flow in a direction perpendicular to the line of heating has a major influence on the simulated circulation patterns and nonhydrostatic pressure deviations near the line of heating. The effect is more pronounced for lower surface temperatures at the heating line. The TKE profiles reveal preferred regions of TKE growth that can be attributed mainly to buoyancy or advection effects.

Keywords: Nonhydrostatic atmospheric model; Vorticity; Turbulence; Buoyancy; Advection.

Introduction

Low-level atmospheric conditions near the flanks of wildland fires are of major concern in fire-fighter safety. The tremendous heating of the atmosphere in the vicinity of a wildland fire generates circulation and turbulence patterns that affect the movement and transport of flames and firebrands (Haines and Smith, 1987). A particular type of circulation pattern, with its associated turbulence structure, is the horizontal roll vortex. Horizontal roll vortices have been observed during a number of wildland

and experimental fires (Schaefer 1957; Church et al. 1980; Haines 1982; Haines and Smith 1987), and simulated in wind-tunnel experiments (Haines and Smith 1983; Smith et al. 1986, 1989).

It has been hypothesized that unburned tree-crown streets found in large forest fires can be attributed to thermally induced roll vortices with sufficiently strong downdrafts (Haines 1982). Horizontal roll vortices along the flanks of firelines have been observed with downdrafts of sufficient strength to break the tops off of jack pine trees (Haines and Smith, 1987). Downdrafts of this magnitude could inhibit the burning of tree crowns adjacent to the firelines. At the same time, firebrands can get caught up in these vortices, be transported to unburned fuels, and initiate new fires. These effects can certainly affect fire-fighter safety.

The development and behavior of horizontal roll vortices, and their associated turbulence structures, are not independent of the ambient dynamic and thermodynamic conditions of the atmospheric boundary layer. Church et al. (1980) describe the basic mechanisms involved in the generation of horizontal roll vortices. Of particular interest is the effect of ambient crossflow components and surface temperature variations on horizontal roll vortex development attributed to buoyancy effects alone, which is one of the mechanisms described by Church et al. (1980).

Although observations and laboratory reproductions of horizontal roll vortices have been reported in the literature, few numerical simulations of horizontal roll vortices induced by wildland fires have been reported (e.g. Luti 1980, 1981). In an effort to extend the previous numerical studies and better understand the physical characteristics of buoyancy-induced horizontal roll vortices and their interactions with the atmospheric boundary layer, we have performed simple two-dimensional numerical simulations of atmospheric conditions near lines of extreme surface heating under varying dynamic and thermal conditions. The numerical results should provide *qualitative* insight into the mean and turbulence

structures associated with buoyancy-induced horizontal roll vortices that may be present in the vicinity of actual firelines.

Nonhydrostatic Model Development

The three-dimensional, hydrostatic, coupled earth/atmospheric model described by McCorcle (1988) and Fast and McCorcle (1990) provided the foundation for the development of the nonhydrostatic boundary-layer model used in this study. This particular model consists of prognostic equations for the horizontal velocity components, potential temperature, specific humidity, and turbulent kinetic energy (TKE). The vertical velocity component and the atmospheric pressure are diagnosed through the continuity and hydrostatic equations, respectively. The model also predicts soil moisture and soil temperature in a manner similar to that described by Mahrt and Pan (1984) and Pan and Mahrt (1987). Several investigators have used this hydrostatic model to examine the diurnal variations of boundary-layer flows (Paegle and McLawhorn 1983; Astling et al. 1985; McCorcle 1988). More recently, the model was used by Fast and McCorcle (1990) to simulate the Great Plains low-level jet.

Many of the underlying assumptions of the hydrostatic model of McCorcle (1988) are violated when simulating phenomena with horizontal scales less than 5 km (Martin and Pielke 1983; Song et al. 1985). In addition, hydrostatic models are inadequate for simulating the strong convection and convergence associated with extreme surface heating characteristic of firelines. This is especially true if simulations of atmospheric circulations near areas of extreme surface heating in complex terrain are performed. In order to resolve small-scale circulations over any type of terrain feature, we transformed the model equations to reflect a non-orthogonal terrain-following coordinate system. In addition, we added a prognostic equation for vertical velocity to make the system nonhydrostatic.

Transformation of the three-dimensional governing equations of McCorcle (1988), using tensor analysis, into the defined two-dimensional non-orthogonal terrain-following coordinate system results in the following equations for the velocity components, potential temperature, and TKE:

$$\begin{aligned} \frac{\partial U}{\partial t} = & -U \frac{\partial U}{\partial x} - \omega \frac{\partial U}{\partial \xi} \frac{C}{\sigma} + \left(\frac{s}{s-z_g} \right)^2 \frac{\partial}{\partial \xi} \left(K_m \frac{\partial U}{\partial \xi} \frac{C}{\sigma} \right) \frac{C}{\sigma} \\ & + f(V-V_g) - f \left(\frac{\partial z_g}{\partial x} \frac{s-\sigma}{s} \right) U + \left(\frac{s-z_g}{s} \right) \omega - \frac{1}{\rho} \frac{\partial p'}{\partial x} \\ & - \frac{1}{\rho} \frac{\partial z_g}{\partial x} \left(\frac{\sigma-s}{s-z_g} \right) \frac{\partial p'}{\partial \xi} \frac{C}{\sigma} \end{aligned} \quad (1)$$

$$\frac{\partial V}{\partial t} = -U \frac{\partial V}{\partial x} - \omega \frac{\partial V}{\partial \xi} \frac{C}{\sigma} + \left(\frac{s}{s-z_g} \right)^2 \frac{\partial}{\partial \xi} \left(K_m \frac{\partial V}{\partial \xi} \frac{C}{\sigma} \right) \frac{C}{\sigma} - f(U-U_g) \quad (2)$$

$$\begin{aligned} \frac{\partial \omega}{\partial t} = & -U \frac{\partial \omega}{\partial x} - \omega \frac{\partial \omega}{\partial \xi} \frac{C}{\sigma} + \left(\frac{s}{s-z_g} \right)^2 \frac{\partial}{\partial \xi} \left(K_m \frac{\partial \omega}{\partial \xi} \frac{C}{\sigma} \right) \frac{C}{\sigma} \\ & - \left(\frac{1}{s-z_g} \right) \frac{\partial z_g}{\partial x} \left(\frac{s}{s-z_g} \right)^2 K_m \frac{\partial U}{\partial \xi} \frac{C}{\sigma} - \left(\frac{s-\sigma}{s-z_g} \right) \frac{\partial^2 z_g}{\partial x^2} U^2 \\ & + \frac{2}{s-z_g} \frac{\partial z_g}{\partial x} U \omega - \frac{1}{\rho} \frac{\partial z_g}{\partial x} \left(\frac{\sigma-s}{s-z_g} \right) \frac{\partial p'}{\partial x} \\ & - \frac{1}{\rho} \left(\frac{\partial z_g}{\partial x} \left(\frac{\sigma-s}{s-z_g} \right) \right)^2 \frac{\partial p'}{\partial \xi} \frac{C}{\sigma} - \frac{1}{\rho} \left(\frac{s}{s-z_g} \right)^2 \frac{\partial p'}{\partial \xi} \frac{C}{\sigma} \\ & - \left(\frac{\sigma-s}{s-z_g} \right) \frac{\partial z_g}{\partial x} f V_g - g \left(\frac{s}{s-z_g} \right) \left(\frac{\rho'}{\rho} \right) \end{aligned} \quad (3)$$

$$\begin{aligned} \frac{\partial \Theta}{\partial t} = & -U \frac{\partial \Theta}{\partial x} - \omega \frac{\partial \Theta}{\partial \xi} \frac{C}{\sigma} + \frac{Q}{c_p} \left(\frac{p}{p'} \right)^{R/c_p} \\ & + \left(\frac{s}{s-z_g} \right)^2 \frac{\partial}{\partial \xi} \left(K_h \frac{\partial \Theta}{\partial \xi} \frac{C}{\sigma} \right) \frac{C}{\sigma} \end{aligned} \quad (4)$$

$$\begin{aligned} \frac{\partial \epsilon}{\partial t} = & -U \frac{\partial \epsilon}{\partial x} - \omega \frac{\partial \epsilon}{\partial \xi} \frac{C}{\sigma} + \left(\frac{s}{s-z_g} \right)^2 \frac{\partial}{\partial \xi} \left(K_\epsilon \frac{\partial \epsilon}{\partial \xi} \frac{C}{\sigma} \right) \frac{C}{\sigma} \\ & + \left(\frac{s}{s-z_g} \right)^2 K_m \left[\left(\frac{\partial U}{\partial \xi} \right)^2 + \left(\frac{\partial V}{\partial \xi} \right)^2 + \left(\frac{\partial \omega}{\partial \xi} \right)^2 \right] \left(\frac{C}{\sigma} \right)^2 \\ & - \left(\frac{s}{s-z_g} \right) \frac{g}{T} K_h \frac{\partial \Theta}{\partial \xi} \frac{C}{\sigma} - \frac{K_m^2}{(c_1 \theta)^4} \end{aligned} \quad (5)$$

Equations (1)-(3) describe the time variation of the two horizontal velocity components, U and V , and the vertical velocity component, ω . The basic processes included on the right-hand sides of Eqs. (1)-(3) are horizontal and vertical advection of the individual wind components, turbulent diffusion of the individual wind components, the Coriolis effect (Eqs. (1) and (2)), horizontal pressure gradient (Eq. (1)), vertical pressure gradient (Eq. (3)) and buoyancy effects (Eq. (3)). Those terms in Eqs. (1)-(3) that contain spatial gradients in the terrain height, z_g , are only applicable for applications over irregular terrain, when special attention must be given to the calculation of horizontal and vertical gradients in the transformed coordinate system. They have been included in the governing equations for this study for completeness. Equation (4) describes the time variation of potential temperature and includes the processes of horizontal and vertical advection, heating due to infrared radiative flux, and turbulent diffusion. The time variation in TKE is described in Eq. (5) and depends on horizontal and vertical advection, turbulent diffusion, production of TKE by vertical shears in the velocity components, production of TKE by buoyancy effects, and dissipation. A list of symbols can be found in the appendix.

Differential heating or cooling induces a pressure gradient that forces the dynamics of a system to change. In this particular study, heating due to fire-type temperatures results in significant pressure variations over very short distances. In order to account for thermally-induced pressure gradients, pressure gradient terms similar to those used by Yamada (1981, 1983) and Heilman and Takle (1991) are added to the U and ω momentum equations. Addition of these terms assumes that the total pressure, p, and density, ρ , can be written as

$$p = p_s + p_h + p' \quad (6)$$

and

$$\rho = \rho_s + \rho_h + \rho' \quad (7)$$

respectively, where p_s and ρ_s are the horizontally homogeneous base-state pressure and density, p_h and ρ_h are the thermally-induced pressure and density perturbations, and p' and ρ' are the nonhydrostatic pressure and density perturbations due to the air motion. It is also assumed that p'/p and ρ'/ρ are much less than unity. The extra pressure-gradient terms in Eqs. (1)-(3) are written as geostrophic wind components, U_g and V_g , which are calculated in the same manner as Yamada (1981).

The dynamic pressure perturbations (p') found in Eqs. (1) and (3) are obtained from a Poisson equation that can be derived by combining Eqs. (1) and (3) with the transformed anelastic continuity equation:

$$\frac{\partial \rho U}{\partial x} + \left(\frac{\partial \rho \omega}{\partial \xi} \right) \frac{C}{\sigma} - \left[\frac{\rho}{s-z_g} \right] \left(U \frac{\partial z_g}{\partial x} \right) = 0 \quad (8)$$

The transformed Poisson equation for the dynamic pressure perturbation is given by

$$\begin{aligned} & \frac{\partial}{\partial x} \left[PU \frac{\partial p'}{\partial x} + PU \frac{\partial z_g}{\partial x} \left(\frac{\sigma-s}{s-z_g} \right) \frac{\partial p'}{\partial \xi} \frac{C}{\sigma} \right] + \\ & \frac{\partial}{\partial \sigma} \left[PW \frac{\partial z_g}{\partial x} \left(\frac{\sigma-s}{s-z_g} \right) \frac{\partial p'}{\partial x} + PW \left(\frac{\partial z_g}{\partial x} \left(\frac{\sigma-s}{s-z_g} \right) \right)^2 \frac{\partial p'}{\partial \xi} \frac{C}{\sigma} \right] + \\ & \frac{\partial}{\partial \sigma} \left[PW \left(\frac{s}{s-z_g} \right)^2 \frac{\partial p'}{\partial \xi} \frac{C}{\sigma} \right] + F = 0 \end{aligned} \quad (9)$$

where

$$F = \frac{\partial (\rho FU)}{\partial x} + \frac{C}{\sigma} \frac{\partial (\rho FW)}{\partial \xi} - \left(\frac{\rho}{s-z_g} \right) \left(U \frac{\partial z_g}{\partial x} \right) \quad (10)$$

and PU, PW, FU, and FW are numerical expressions involving U and ω . As with Eqs. (1)-(5), those terms

involving spatial gradients of the terrain height are only applicable for applications over irregular terrain.

The TKE equation, Eq. (5), contains mechanical production terms that only involve vertical shears of the horizontal and vertical winds. The conditions simulated in this study typically involve horizontal shears of the vertical winds that are larger than those existing under normal atmospheric boundary-layer conditions. However, in the vicinity of a source of heating like that simulated in this study, the production of turbulence energy by mechanical means (shears in the wind field) is much less important than the production of turbulence energy by buoyancy effects. For this reason and for *qualitatively* examining the turbulence structures above heating lines, the TKE production terms used in typical boundary-layer studies are utilized in Eq. (5). When the production of turbulence by buoyancy effects does not dominate and significant horizontal shears in the wind field are present, the simulation of turbulence production should include horizontal gradients of the velocity components. Under such conditions, the calculation of horizontal gradients requires a model grid structure with horizontal resolution comparable to the vertical resolution. However, in this study, emphasis is placed on the turbulence structure where buoyancy effects are large and mechanical effects due to horizontal shears in the wind components are small in comparison.

Computational Processes

Numerical Methods

Both finite-difference and finite-element techniques are used to approximate the governing prognostic equations. Advection, pressure gradient, TKE shear production, and TKE buoyancy production terms are expressed in finite-difference form. A Galerkin finite-element technique is used to represent vertical diffusion effects. This technique controls the problem of nonlinear computational instability associated with aliasing errors. The numerical representation of local rates of change in the modeled variables takes the form of the Crank-Nicholson finite-difference method.

The Poisson equation for dynamic pressure perturbations is solved at each time step by an iterative successive over-relaxation procedure. The iteration at each time step is continued until values of the perturbation pressures between successive iterations change by no more than 0.001%.

Model Domain

The computational domain spans a 2.0 km wide (x-

direction) by 1.8 km high (ξ -direction) vertical plane. Horizontal homogeneity in the y -direction is assumed for all variables. The horizontal grid spacing is 50 m. The vertical grid spacing from the surface up to about 100 m is logarithmic, with a minimum spacing of 0.27 m just above the surface. Above 100 m, the grid spacing is constant (~ 190 m). We used a total of 41 grid points in the horizontal and 16 grid points in the vertical. The fine vertical resolution of the model near the surface allows for a detailed description of mean and turbulent processes (vertical advection, production and dissipation of TKE, etc.) just above the ground where atmospheric variables typically show extensive vertical variations. However, the fine vertical grid resolution necessitates the use of a 0.05 s to 0.1 s time step to solve the prognostic equations. For this study, we assumed level terrain height. The transformation of the governing equations to a coordinate system that becomes non-orthogonal when applied over complex terrain will allow for future studies of terrain effects on fire vortex development.

Boundary and Initial Conditions

Extreme surface heating along a line (homogeneous in the y -direction) is represented by constant potential temperatures of 900°K and 1500°K at the surface grid points in the middle of the modeled x - z vertical plane. (Hereafter, references to lines of heating correspond to heating lines oriented in the y -direction. The lines of heating appear as points in the modeled x - z vertical plane). The surface potential temperatures of 900°K and 1500°K correspond to blackbody radiative fluxes of 37 kW m⁻² and 287 kW m⁻², respectively, assuming surface emissivities of one. These heat source specifications allow for an examination of the boundary-layer dynamics that evolve from a surface heat source as opposed to a volume heat source embedded in the boundary layer. The model derives surface potential temperatures at other locations from surface soil temperatures calculated with a soil heat-flux equation. At the atmosphere/soil interface, the thermodynamic energy equation and the soil heat-flux equation are coupled with a surface heat-balance equation to provide the means for calculating the physical forcing due to radiative heating and cooling. The model also calculates surface-layer values for the mean and turbulent variables from the relations established by Paulson (1970), Businger et al. (1971), and Mellor and Yamada (1974). Zero-gradient conditions are assumed for the dynamic pressure perturbations at the surface.

At the model top, we used a specified geostrophic wind field as a boundary condition for the horizontal velocity components and set the vertical wind component at the model top to zero. Zero-gradient boundary

conditions at the model top are used for potential temperature, TKE, and dynamic pressure perturbations. To insure horizontal homogeneity at the lateral boundaries, we used zero-gradient conditions for all variables except the dynamic pressure deviations; they were set to zero at the boundary grid points. Simulations were monitored so that the movement of atmospheric features generated by the surface heating line remained sufficiently distant from the lateral and top boundaries of the model domain where zero-gradient conditions were employed.

The model is initialized for each simulation with a constant potential temperature of 298°K, except at the specified line of heating. The initial wind component in the x -direction, U , is assumed to be logarithmic from the surface to the model top. Friction velocities (u_*) of 0.0, 0.05, 0.1, and 0.2 m s⁻¹ are used for the velocity component in the x -direction. These initial friction velocities produce initial model-top velocities of 0.0 m s⁻¹, 1.43 m s⁻¹, 2.86 m s⁻¹, and 5.73 m s⁻¹, respectively. The friction velocity of the y -component of the initial wind field, V , is always given a value of 0.2 m s⁻¹. Initial conditions for TKE are obtained from level two of the Mellor-Yamada turbulence hierarchy (Mellor and Yamada 1974). The soil-layer temperatures are initialized at 298°K, and a dry soil layer is assumed.

Numerical Results

Figure 1 shows the effect of an ambient U -velocity on the two-dimensional wind fields after 90 s of simulation time with a surface potential temperature of 900°K at $x=1000$ m. With no ambient U -velocity, strong flow toward the line of heating appears at low altitudes on both sides of the heating line (Fig. 1a). An analysis of the U -velocity profiles reveals maximum inflow speeds of 10 m s⁻¹ at heights of 5.5 m above the surface at $x=950$ m and $x=1050$ m. The updraft over the region of high surface temperature is also vigorous, reaching a maximum speed of 10.7 m s⁻¹ at a height of 298 m. Overall, the updraft region extends to about 700 m above the surface. Horizontal vortices on both sides of the updraft region are prominent. At $x=900$ m and $x=1100$ m, the downdrafts reach their maximum speeds of 3.7 m s⁻¹ at a height of 298 m. The vortex behavior is of sufficient strength to cause the downdrafts to exceed speeds of 1 m s⁻¹ at heights as low as 10 m above the surface.

Figure 1b shows results for a logarithmic, weak ambient U -velocity (initial $u_* = 0.05$ m s⁻¹ and maximum ambient U -velocity = 1.43 m s⁻¹ at the model top). Symmetric horizontal vortices near the region of heating never develop, although the heating is sufficient to force an inflow that overcomes the ambient flow at heights below 15 m at $1050 \text{ m} < x < 1100 \text{ m}$, thus producing a

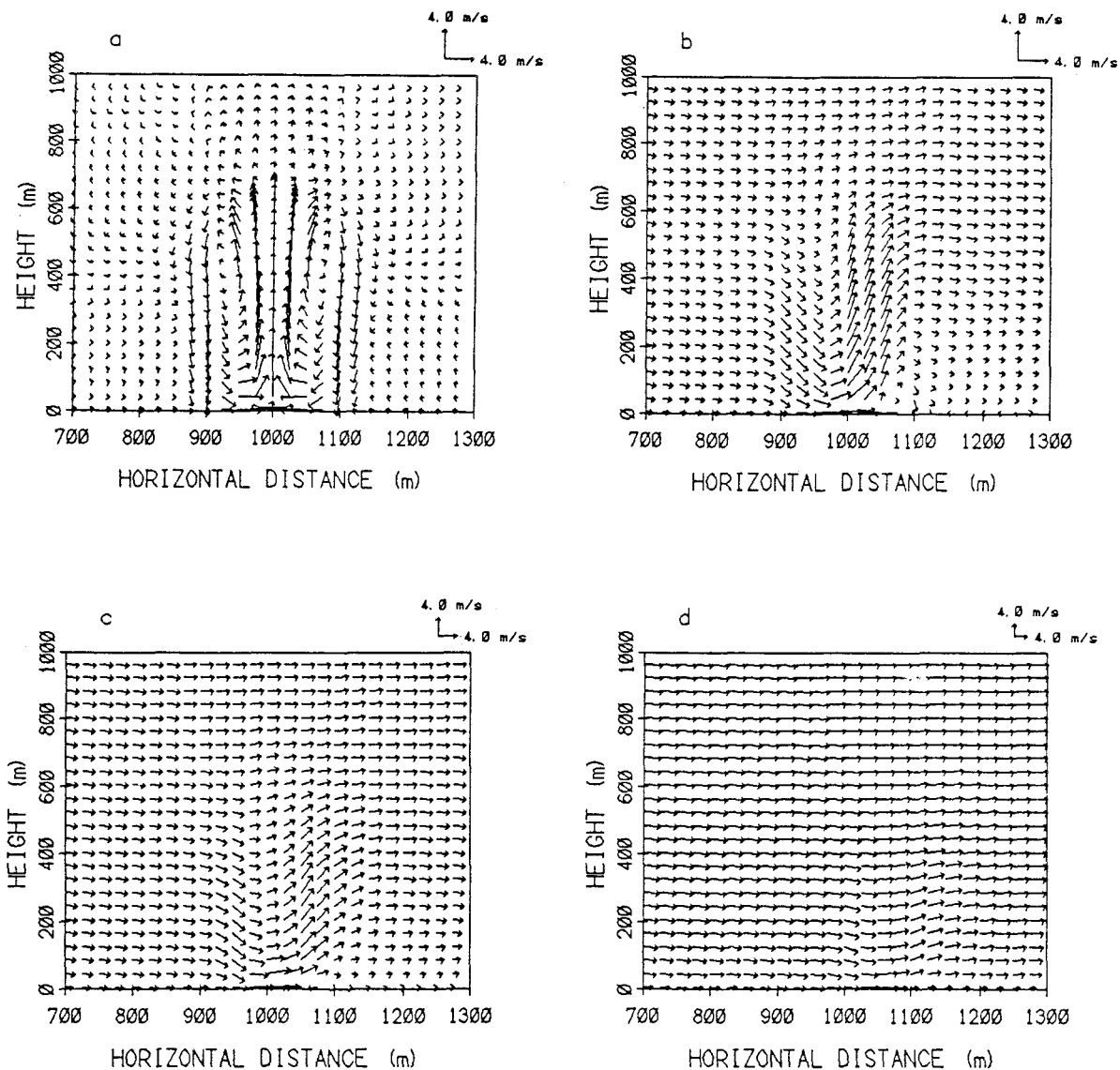


Figure 1. Simulated wind fields associated with a surface potential temperature of 900°K at $x=1000\text{ m}$ with (a) no ambient U-velocity, and light ambient U-velocities resulting from initial friction velocities of (b) 0.05 m s^{-1} , (c) 0.1 m s^{-1} , and (d) 0.2 m s^{-1} .

low-level vortex. Whereas the U-velocity was nearly zero at $x=1000\text{ m}$ with no ambient wind, in this case it reaches a maximum of 3.8 m s^{-1} at $x=1000\text{ m}$. A wake effect develops below 50 m on the downwind side of the surface heating, where wind speeds are very light. At higher altitudes, the wind field develops a wave in response to the surface heating at $x=1000\text{ m}$, with the updraft region extending downwind to $x=1075\text{ m}$ (interpolated). A reduced maximum downdraft speed of about 1.5 m s^{-1} appears at $x=950\text{ m}$ at 110 m above the surface.

When the ambient U-velocity is increased, resulting

in an initial friction velocity of 0.1 m s^{-1} (maximum initial U-velocity = 2.86 m s^{-1}), the wave pattern is diminished (Fig. 1c). However, the low-level vortex downwind of the heating line still persists. A further increase in the ambient U-velocity (initial friction velocity = 0.2 m s^{-1} and maximum initial U-velocity = 5.73 m s^{-1}) nearly eliminates the wave pattern, terminates the low-level buoyancy-induced inflow downwind of the heating line ($x > 1000\text{ m}$), and destroys the low-level downwind vortex (Fig. 1d).

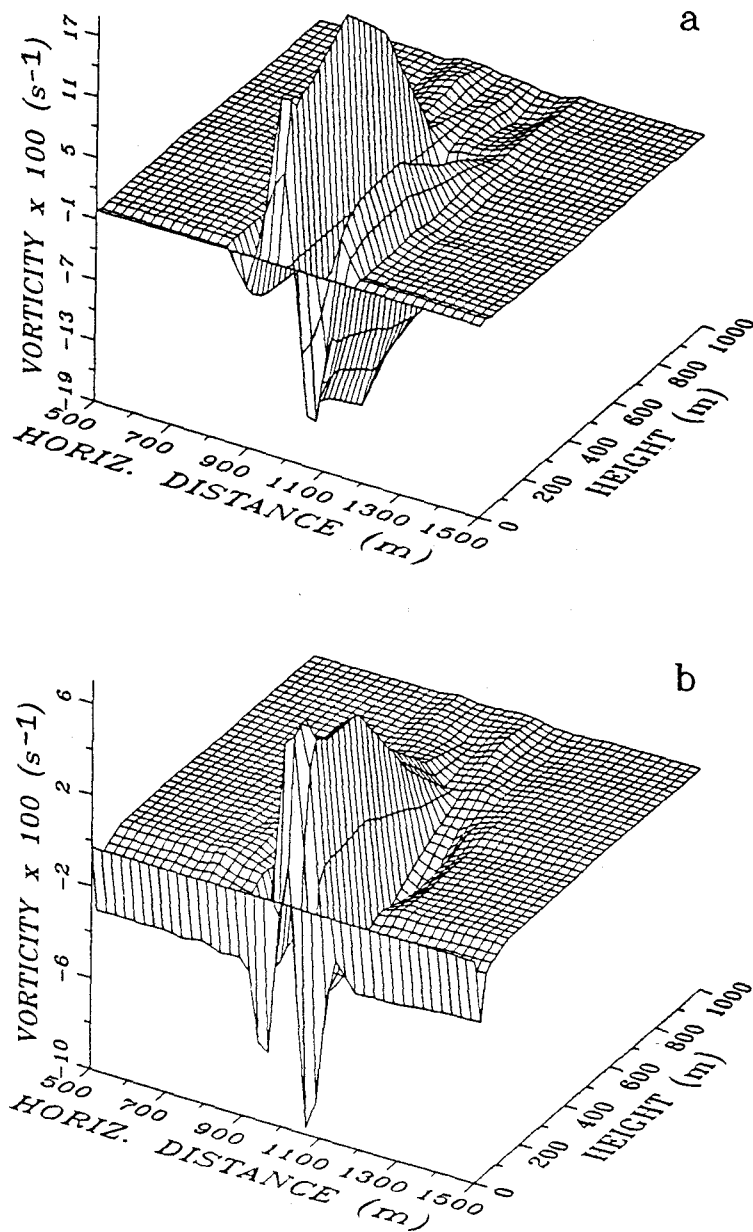


Figure 2. Simulated vorticity fields associated with a surface potential temperature of 900°K at $x=1000$ m with (a) no ambient U-velocity, and (b) a light ambient U-velocity resulting from an initial friction velocity of 0.1 m s^{-1} .

Figure 2 shows the vorticity in the simulated wind fields of Figs. 1a and 1c. Positive and negative vorticity in the figures correspond to counterclockwise and clockwise circulations, respectively. With no ambient U-velocity, the symmetric vortices adjacent to the heating line are characterized by relatively strong vorticity (Fig. 2a). When the ambient U-velocity is increased ($u_a=0.1$ m s^{-1}), the vorticity values are reduced everywhere except near the surface where shear effects are stronger (Fig. 2b). The low-level vortex downwind of the heating

line shows up as a negative vorticity maximum (~ -0.09 s^{-1}).

Figure 3 shows the effects of the same ambient wind conditions as in Fig. 1, but with a surface temperature of 1500°K at the line of heating. The circulations in the vortices surrounding the heating line are more prominent and vigorous than in the 900°K surface temperature case with no ambient U-velocity (Fig. 3a). Maximum inflow speeds reach 14.7 m s^{-1} at heights of 2 m above the surface at $x=950$ m and $x=1050$ m. The updraft speeds over the

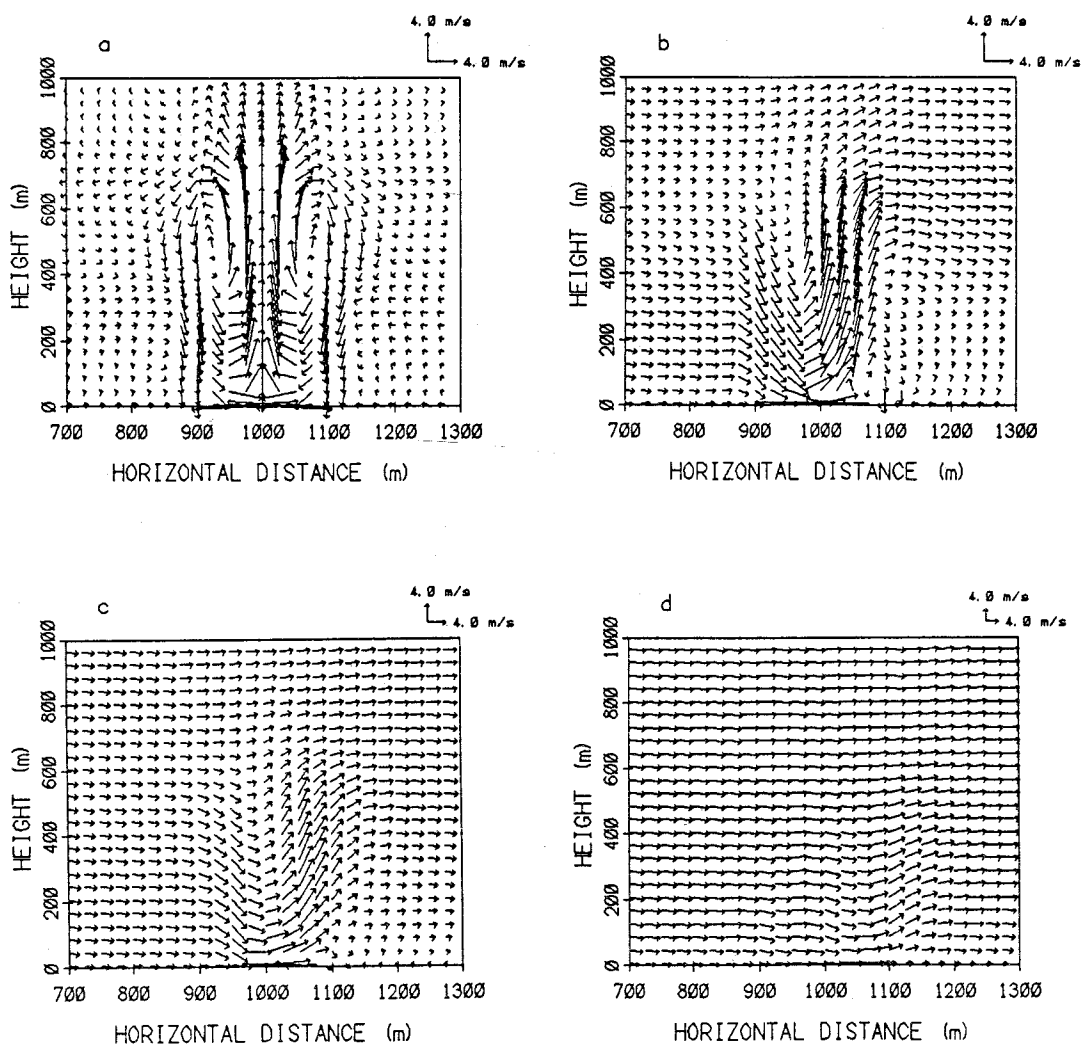


Figure 3. Same as Fig.1 except for a surface potential temperature of 1500°K.

line of heating are also greater, reaching a maximum of 21.5 m s^{-1} at a height of 487 m. The updraft region extends upward to about 900 m. Maximum downdraft speeds of 5.8 m s^{-1} appear at heights of 298 m above the surface at $x=900 \text{ m}$ and $x=1100 \text{ m}$.

When the ambient U-velocity is increased as in the 900°K surface temperature cases, the increased surface temperature at the heating line cannot preserve the prominent vortex behavior (Figs. 3b, 3c, and 3d). However, the buoyancy-induced low-level inflow downwind of the heating line is of sufficient strength to create a low-level vortex below 100 m at $1050 \text{ m} < x < 1100 \text{ m}$ when the initial friction velocities are 0.05 m s^{-1} and 0.1 m s^{-1} . The light ambient U-velocities and their interaction with the thermally-induced flow result in maximum horizontal wind speeds directly over the heating line at a height of 2 m above the surface (Figs. 3b and 3c). Furthermore, the ambient U-velocities are strong enough to spread the updraft regions downwind a considerable distance, placing them directly over the low-level recirculation zones.

An upper-level jet, with its core centered about 600 m above the surface, develops downwind of the heating line ($x > 1100 \text{ m}$) when the initial friction velocity is 0.05 m s^{-1} (Fig. 3b). The occurrence of such a jet downwind of a fireline could potentially carry hot air downwind and create a stable atmospheric layer below it, where turbulence would tend to be suppressed. Such an occurrence depends on the extent of radiative cooling and turbulent mixing of the elevated hot plume, which would act to diminish the stability of the layer below it. Maximum updraft speeds directly over the heating line are reduced to 7.7 m s^{-1} and 2.1 m s^{-1} when the initial friction velocities are increased to 0.05 m s^{-1} and 0.1 m s^{-1} , respectively. Downdrafts are most prominent just upwind of the heating line for these scenarios, although they are at least 50% weaker than in the no-ambient U-velocity case. Increasing the initial friction velocity to 0.2 m s^{-1} terminates the buoyancy-induced inflow downwind of the heating line and prevents the development of the low-level vortex (Fig. 3d).

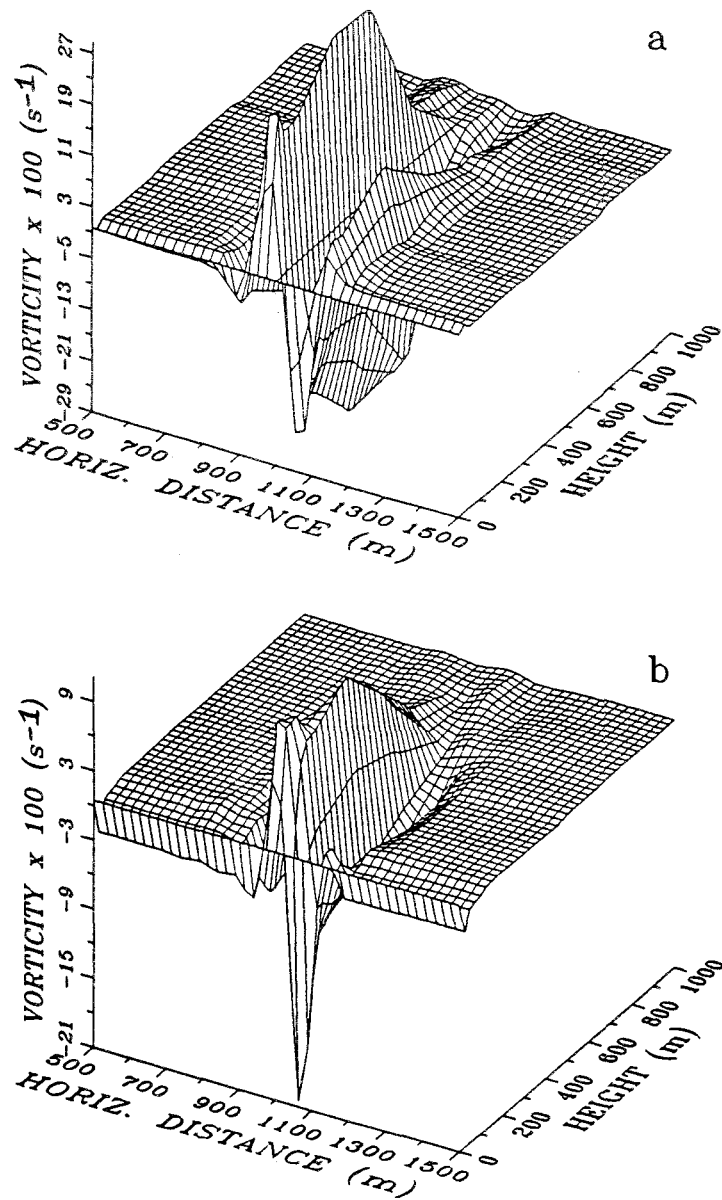


Figure 4. Same as Fig. 2 except for a surface potential temperature of 1500°K.

Figure 4 shows the vorticity fields corresponding to the wind fields shown in Figs. 3a and 3c. As expected, vorticity magnitudes are larger when the surface temperature at the heating line is increased from 900°K to 1500°K (Fig. 4a). The low-level vortex downwind of the heating line when a light ambient U-velocity is present produces a prominent low-level vorticity "spike" (Fig. 4b), with a value of nearly -0.21 s^{-1} . Vorticity in this low-level vortex is more than twice the vorticity in the low-level vortex simulated in the 900°K surface temperature case (Fig. 2b). Results from the 900°K and the 1500°K surface temperature simulations suggest the importance of surface temperature and ambient crossflow conditions in producing low-level vortices downwind of heating

lines. Similar vortices that develop along the flanks of firelines can be a potential hazard to fire fighters if flames and firebrands are caught in the vortices.

The wind-field results from these simulations show qualitative agreement with previous studies. For the cases of no ambient wind, the vortex pair development is quite similar to the wind-tunnel observations of Haines and Smith (1983) and Smith et al. (1986, 1989). Haines observed evidence of horizontal roll vortices in lateral crown-fire spread and hypothesized that a single horizontal roll vortex on the perimeter of a burning region tends to bring cooler ambient air into the vortex's downdraft and to inhibit the spread of fire outward from the perimeter. This behavior supports the uncharred

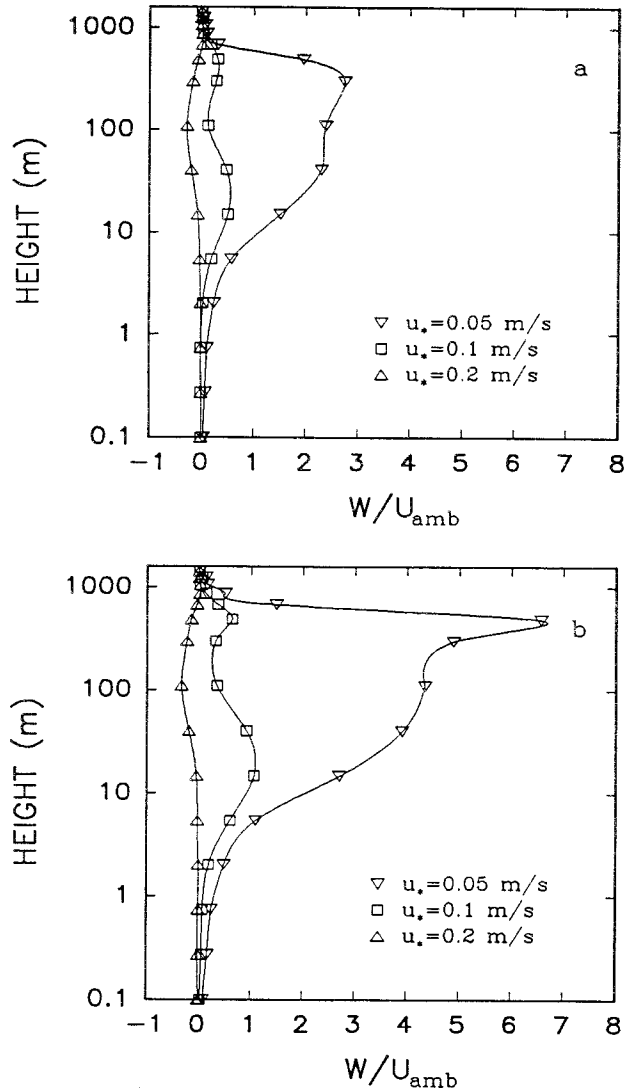


Figure 5. Simulated profiles of the ratio of the vertical wind component (W) over the heating line at $x=1000$ m to the ambient horizontal wind component (U_{amb}) for surface potential temperatures of (a) 900°K and (b) 1500°K .

tree-trunk patterns observed by Simard et al. (1983). As seen in Figs. 1a and 3a, the wind field with no ambient U -velocity is characterized by low-level inflow into the region of heating and induced downdrafts at about 100 m from the region of heating. The simulated wind fields with a light ambient U -velocity also show a behavior quite similar to the wind tunnel results of Smith and Haines (1991). In their experiments, a flow component perpendicular to the heating line produced a low-level vortex on the downwind side of the heating line.

The effects of ambient crossflows and surface temperatures on the circulation patterns over the line of heating can be quantified by comparing the kinetic energy of the ambient crossflow with the kinetic energy of the convective column above the heating line. This

analysis is similar to the work of Byram (1959), who derived energy-criterion equations that can be used to calculate the energetics of circulation patterns over burning surfaces. Byram's equations are useful for comparing the power of the wind field at any height above a burning surface with the rate at which thermal energy is converted to kinetic energy in the convection column above the flames. When the kinetic energy (or wind speeds) of the ambient wind field is greater than or equal to the kinetic energy (or wind speeds) of rising air within the convective column, a forced-convection circulation exists. A free-convection type of circulation exists when the vertical wind speeds within the convective column exceed the ambient horizontal wind speeds. For the simulations in this study, ratios of the vertical and

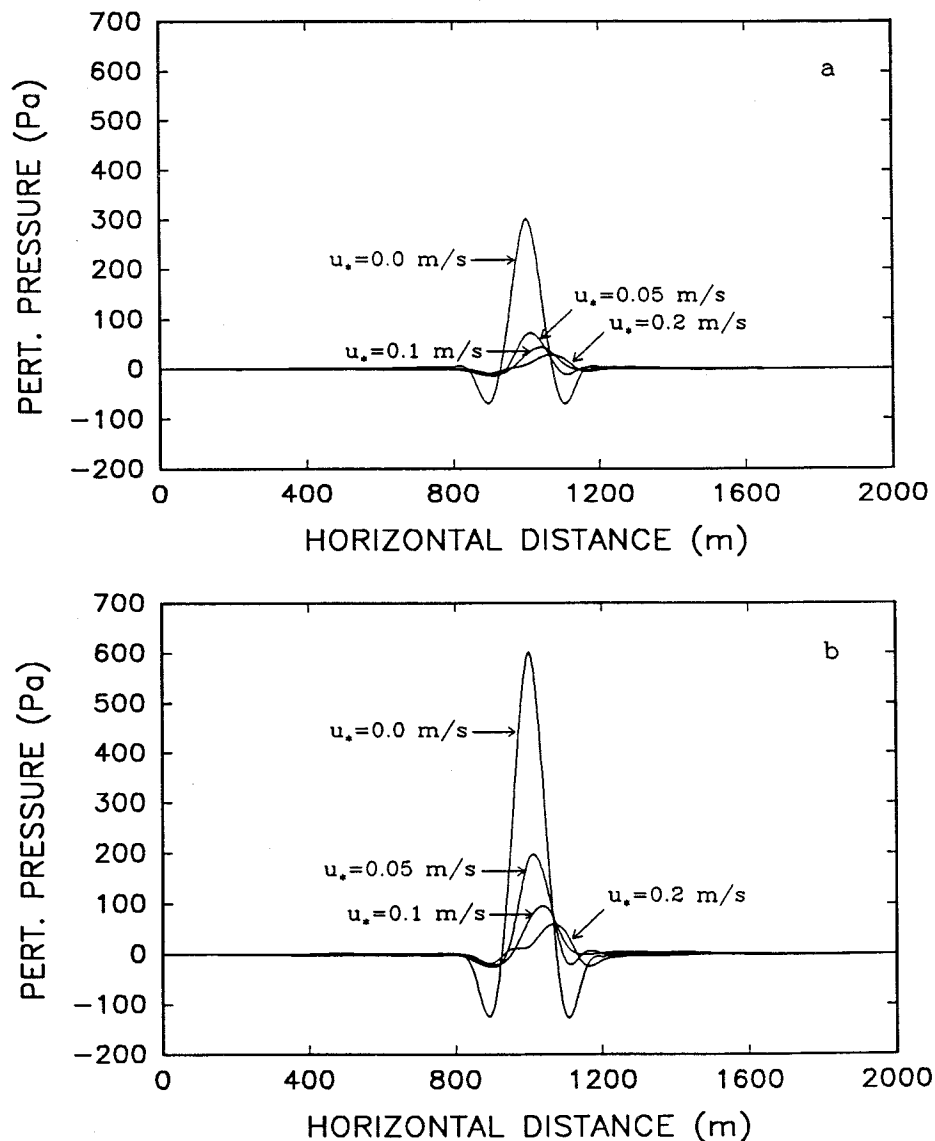


Figure 6. Ambient U-velocity effects on the simulated dynamic perturbation pressures at 2 m above the surface for surface potential temperatures of (a) 900°K and (b) 1500°K.

horizontal wind speeds were calculated for the different crossflow and surface potential temperature conditions. Profiles of these ratios are shown in Fig. 5. For both the 900°K (Fig. 5a) and 1500°K (Fig. 5b) cases, ambient crossflows characterized by friction velocities greater than 0.1 m s^{-1} result in circulations over the heating line that are controlled mainly by the crossflows. When the initial friction velocity is reduced to 0.05 m s^{-1} , the vertical wind speeds over the heating line exceed the ambient crossflow wind speeds at heights between 5 m and 900 m. Increasing the surface potential temperature from 900°K to 1500°K at the heating line increases the maximum value of the ratio of wind speeds from 2.7 to 6.6. The height of the maximum ratio also increases as

the surface potential temperature increases. When the ambient crossflow speeds are sufficiently large, the simulated region of maximum updrafts is displaced downwind a considerable distance, and wind vectors with a downward velocity component actually exist directly over the heating line (Figs. 1d and 3d). These downward velocity components can be observed in Figs. 5a and 5b when the initial friction velocity is 0.2 m s^{-1} .

Figure 6 shows the effects of surface temperatures at the heating line and ambient crossflow conditions on dynamic (nonhydrostatic) perturbation pressures that develop in response to the thermally-induced flow at a height of 2 m. Clearly, the magnitudes and horizontal gradients of the perturbation pressures are greatly re-

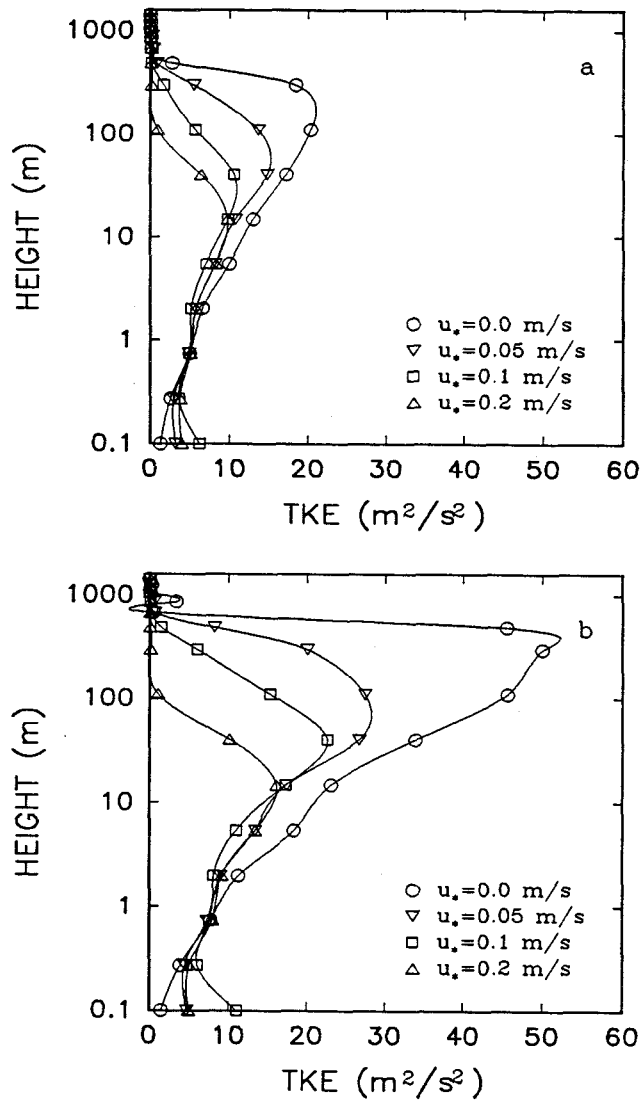


Figure 7. Ambient U-velocity effects on the simulated TKE profiles over the heating line at $x=1000$ m for surface potential temperatures of (a) 900°K and (b) 1500°K.

duced when the surface temperature is lower and a light ambient U-velocity is present. The pressure patterns are symmetric for the no-ambient-wind cases, with maximum perturbation pressures of 301 Pa and 601 Pa directly over the heating lines for surface temperatures of 900°K (Fig. 6a) and 1500°K (Fig. 6b), respectively, at the heating lines. Maximum perturbation pressures do not appear over the lines of heating when an ambient wind is present; they are displaced downwind, greatly reduced, and no longer symmetric. The simulated perturbation pressure patterns shown in Fig. 6 remain fairly constant up to about 15 m. Above 15 m, the perturbation pressure magnitudes decrease to zero at heights between 700 m and 1000 m. The presence of a light ambient U-velocity leads to convergence and divergence values

near the line of heating that are much smaller than the values present when there is no ambient wind. This, in turn, leads to smaller perturbation-pressure magnitudes derived from the atmospheric continuity equation.

The presence of an ambient U-velocity also affects the turbulence structure. Over the line of heating, buoyancy production of TKE dominates and generates the TKE profiles shown in Figs. 7a and 7b. Maximum TKE values increase in magnitude and appear at increasing heights above the surface as the ambient U-velocity decreases to zero. A diminishing advective crossflow allows the instability to increase over the line of heating, and thus, increases the potential for buoyancy generation of turbulence energy. An increase in surface potential temperature from 900°K to 1500°K results in maximum

TKE values that are nearly doubled over the heating line for all the ambient U-velocity cases. Above the surface layer at $x < 950$ m and $x > 1050$ m, TKE values are much smaller than the values over the heating line when no ambient U-velocity is present. In these regions, buoyancy production of TKE is small. However, advective effects when an ambient U-velocity is present produce downwind TKE maxima near 100 m above the surface.

The simulations performed in this study used an ambient adiabatic atmosphere. The turbulence structure that develops in response to the surface heating is affected by the ambient stability of the simulated atmosphere. Simulations of the turbulence structure under ambient stable conditions (not shown) indicate an increase in turbulence just below the rising capping inversion over the line of heating. This effect is most pronounced with no ambient crossflow. Diffusion of turbulent energy upward is inhibited at the inversion base, resulting in an increase in turbulence there. As the inversion base is eroded from below by the transfer of heat upward, turbulent energy can move to higher levels in the boundary layer.

The overall effect of turbulence is to diminish spatial gradients in the atmospheric variables through the process of turbulent diffusion. In the horizontal roll vortex regions where significant gradients can be found, turbulence acts to destroy the organized structures of the vortices by extracting energy from them. This energy extraction process manifests itself through an increase in TKE, which tends to increase turbulent diffusion if gradients in the mean atmospheric variables are present. After turbulence energy has been generated, it is passed from the larger-scale eddies to the smaller-scale eddies and then dissipated. Because of this energy-cascade process, organized flow phenomena like horizontal roll vortices are a source of energy for small-scale turbulent eddies.

Summary and Conclusions

A two-dimensional nonhydrostatic numerical model has been used to simulate mean and turbulent characteristics near lines of extreme surface heating. Model simulations of ambient crossflow effects and varying surface temperatures have been performed. A qualitative analysis of the results has generated the following conclusions.

- (a) Ambient crossflows and surface temperatures along lines of heating play a significant role in affecting the development of buoyancy-induced symmetric horizontal roll vortices. Larger surface temperatures at the heating lines produce more vigorous vortex

circulations. The presence of a light ambient crossflow completely inhibits the development of these vortices for the temperature scenarios performed in this study. However, the presence of a sufficiently light ambient crossflow results in the development of a low-level vortex with significant vorticity immediately downwind of the heating line. If this type of buoyancy-induced vortex were to develop along the flank of a fireline, with flames and firebrands caught in the circulation, fire fighters could be endangered. The simulations also indicate the development of an upper-level jet downwind of the heating line when a light ambient crossflow is present.

- (b) Nonhydrostatic dynamic pressure perturbations near the region of surface heating reflect ambient crossflow conditions and surface potential temperature variations. Higher surface temperatures generate more low-level flow convergence, resulting in larger dynamic pressure perturbations. An ambient crossflow greatly reduces the magnitudes of the pressure perturbations and tends to transport the pressure perturbation maxima and minima downwind.
- (c) The two-dimensional turbulence structure indicates a significant interaction of ambient crossflows with the turbulent energy and the generation of turbulence due to buoyancy. Directly over the heating line, turbulence energy tends to increase as the ambient crossflow diminishes and the surface temperature increases. The level of maximum energy also increases under these conditions. The turbulence structure is controlled, to a large extent, by the ambient stability of the atmosphere.

We have attempted to investigate some fundamental processes governing the generation of horizontal roll vortices by buoyancy effects, which is one of the crucial mechanisms involved in creation of roll vortices during actual fire episodes (Church et al. 1980). The model simulation results in this study should be viewed qualitatively, in light of the two-dimensional nature of the model and the lack of parameterized flame dynamics in a surface layer of trees. Nevertheless, the simulations indicate the importance of flow perpendicular to heating lines, surface temperature variations, and atmospheric turbulence in affecting updraft and downdraft conditions associated with buoyancy-induced horizontal roll vortices. While ambient crossflow conditions and surface temperature variations existing around actual firelines

are certainly more erratic than the conditions used in these simulations, the present results suggest important qualitative tendencies of the atmosphere near regions of extreme surface heating that should be noted. These tendencies may be of significance for fire-fighter safety.

Further two-dimensional modeling studies are needed to examine fundamental processes in the atmospheric boundary layer when multiple heating lines are present. In addition, the ability of the model to simulate atmospheric conditions over two-dimensional terrain features will allow for future simulations of buoyancy-induced horizontal roll vortex development over irregular terrain and changes in surface roughness. Three-dimensional modeling studies are needed to investigate the interaction of the mechanisms of horizontal vorticity reorientation and stretching and vertical vorticity con-

centration and amplification, as outlined by Church et al. (1980), with the buoyancy mechanism investigated in this study. Finally, ongoing and future modeling studies such as these beg for observational verification. In particular, measurements of updraft and downdraft wind speeds, turbulent wind fluctuations, and sensible heat fluxes are needed in the convective columns above extreme surface heating sources, as well as in the regions adjacent to the convective columns where buoyancy-induced horizontal roll vortices typically appear. Before significant quantitative results and conclusions can be made regarding buoyancy-induced horizontal roll vortices over firelines in regions of flat or irregular terrain, observational data (both mean and turbulent) will be needed in support of model results.

APPENDIX

List of Symbols

C	Constant in the vertical coordinate ξ definition
C_p	Specific heat at constant pressure
c_1	Constant in the dissipation term of the TKE equation
e	Turbulent kinetic energy
f, f	Coriolis parameters
g	Gravitational acceleration
K_s	Diffusion coefficient for TKE
K_h	Heat diffusivity
K_m	Momentum diffusivity
ℓ	Vertical mixing length
p	Total atmospheric pressure
p_h	Thermally-induced hydrostatic pressure component
p_s	Base-state hydrostatic pressure component
p_0	Reference surface pressure (10^5 Pa)
p'	Nonhydrostatic pressure perturbation
Q	Heating due to infrared radiative flux
R	Gas constant for dry air
s	Height of model top
T	Temperature
t	Time
U	Mean velocity component in x-direction
U_s	Thermally-induced pressure gradient in y-direction, expressed as a geostrophic velocity
u_s	Friction velocity
V	Mean velocity component in y-direction
V_s	Thermally-induced pressure gradient in x-direction, expressed as a geostrophic velocity
x, z	Orthogonal Cartesian coordinates
z_s	Terrain height
θ	Potential temperature
$\xi = C \ln(\sigma/0.1)$	Transformed vertical coordinate in logarithmically spaced portion of model grid
ρ	Total atmospheric density
ρ_h	Thermally-induced density component
ρ_s	Base-state density component
ρ'	Dynamic density perturbation
$\sigma = s(z - z_s)/(s - z_s)$	Vertical coordinate in the non-orthogonal coordinate system
ω	Mean velocity component in ξ -direction

References

- Astling, E. G., J. Paegle, E. Miller, and C. J. O'Brien. 1985. Boundary layer control of nocturnal convection associated with a synoptic scale system. *Monthly Weather Review* 113:540-552.
- Businger, J. A., J. C. Wyngaard, Y. Izumi, and E. F. Bradley. 1971. Flux-profile relationships in the atmospheric surface layer. *Journal of the Atmospheric Sciences* 28:181-189.
- Byram, G. M. 1959. Forest fire behavior. In: *Forest Fire: Control and Use*, (ed. K. P. Davis), McGraw-Hill Book Company, Inc.
- Church, C. R., J. T. Snow, and J. Dessens. 1980. Intense atmospheric vortices associated with a 1000 MW fire. *Bulletin of the American Meteorological Society* 61:682-694.
- Fast, J. D., and M. D. McCorcle. 1990. A two-dimensional numerical sensitivity study of the Great Plains low-level jet. *Monthly Weather Review* 118:151-163.
- Haines, D. A. 1982. Horizontal roll vortices and crown fires. *Journal of Applied Meteorology* 21:751-763.
- Haines, D. A. and M. C. Smith. 1983. Wind tunnel generation of horizontal roll vortices over a differentially heated surface. *Nature* 306:351-352.
- Haines, D. A. and M. C. Smith. 1987. Three types of horizontal vortices observed in wildland mass and crown fires. *Journal of Climate and Applied Meteorology* 26:1624-1637.
- Heilman, W. E. and E. S. Takle. 1991. Numerical simulation of the nocturnal turbulence characteristics over Rattlesnake Mountain. *Journal of Applied Meteorology* 30:1106-1116.
- Luti, F. M. 1980. Transient flow development due to a strong heat source in the atmosphere. Part 1: Uniform temperature source. *Combustion Science and Technology* 23:163-175.
- Luti, F. M. 1981. Some characteristics of a two-dimensional starting mass fire with cross flow. *Combustion Science and Technology* 24:25-33.
- Mahrt, L. and H. Pan. 1984. A two-layer model of soil hydrology. *Boundary Layer Meteorology* 29:1-20.
- Martin, C. L. and R. A. Pielke. 1983. The adequacy of the hydrostatic assumption in sea breeze modeling over flat terrain. *Journal of the Atmospheric Sciences* 40:1472-1481.
- McCorcle, M. D. 1988. Simulation of surface-moisture effects on the Great Plains low-level jet. *Monthly Weather Review* 116:1705-1720.
- Mellor, G. L. and T. Yamada. 1974. A hierarchy of turbulence closure models for planetary boundary layers. *Journal of the Atmospheric Sciences* 31:1791-1806.
- Paegle, J. and D. W. McLawhorn. 1983. Numerical modeling of diurnal convergence oscillations above sloping terrain. *Monthly Weather Review* 111:67-85.
- Pan, H. and L. Mahrt. 1987. Interaction between soil hydrology and boundary-layer development. *Boundary Layer Meteorology* 38:185-202.
- Paulson, C. A. 1970. The mathematical representation of wind speed and temperature profiles in the unstable atmospheric surface layer. *Journal of Applied Meteorology* 9:857-861.
- Schaefer, V. J. 1957. The relationship of jet streams to forest fires. *Journal of Forestry* 55:419-425.
- Simard, A. J., D. A. Haines, J. S. Frost, and R. W. Blank. 1983. The Mack Lake fire. *USDA Forest Service, General Technical Report NC-83*, 31 p.
- Smith, M. C. and D. A. Haines. 1991. Simulation of the collapse of horizontal vortex pairs observed in wildland fires. Unpublished Manuscript, North Central Forest Experiment Station, East Lansing, MI.
- Smith, M. C., D. A. Haines, and W. A. Main. 1986. Some characteristics of longitudinal vortices produced by line-source heating in a low-speed wind tunnel. *International Journal of Heat and Mass Transfer* 29:59-68.
- Smith, M. C., D. A. Haines, and W. A. Main. 1989. Growth of buoyancy-induced longitudinal vortex pairs in a laminar flow. *International Journal of Heat and Mass Transfer* 32:1879-1885.
- Song, J. L., R. A. Pielke, M. Segal, R. W. Arritt, and R. C. Kessler. 1985. A method to determine nonhydrostatic effects within subdomains in a mesoscale model. *Journal of the Atmospheric Sciences* 42:2110-2120.
- Yamada, T. 1981. A numerical simulation of the nocturnal drainage flow. *Journal of the Meteorological Society of Japan* 59:108-122.
- Yamada, T. 1983. Simulations of nocturnal drainage flows by a q^2 - \mathcal{L} turbulence closure model. *Journal of the Atmospheric Sciences* 40:91-106.